Effect of autogenous shrinkage on microcracking and mass transport properties of concrete containing supplementary cementitious materials

M.H.N. Yio, M.J. Mac, Y.X. Yeow, H.S. Wong*, N.R. Buenfeld

Centre for Infrastructure Materials, Department of Civil and Environmental Engineering, Imperial College London, SW7 2AZ, United Kingdom

Abstract

It is well-known that supplementary cementitious materials (SCMs) and low water-to-binder (w/b) ratio increase autogenous shrinkage, but the impact on microcracking and long-term transport properties is less understood. This paper examines the effect of microcracking induced by autogenous shrinkage on transport properties of concretes cured up to ~3.6 years. Variables include SCM type (9% SF, 70% GGBS), w/b ratio (0.20-0.45), maximum-aggregate-size (MSA: 5-20 mm) and shrinkage reducing admixture (SRA). Oxygen diffusivity, permeability and water sorptivity were correlated with microcracks characterised using laser scanning confocal microscopy and 3D X-ray microtomography. Results show greater microcracking in mixes containing SCMs, low w/b ratio and large MSA. At the same w/b ratio and binder type, strong positive correlations are observed between transport and microcracking with increasing MSA, confirming the negative impact of autogenous shrinkage. SRA was effective in reducing these effects. The significance is compared with drying shrinkage and implications for durability are discussed.

Keywords: Shrinkage (C); microcracks (B); transport properties (C); durability (C); high performance concrete (E)

1 Introduction

The use of concretes containing supplementary cementitious materials (SCMs) and low water-to-binder (w/b) ratio is becoming increasingly common due to their improved mechanical properties, enhanced durability and sustainability. For example, high-performance concretes (HPC) are produced with a very low w/b ratio (typically ≤ 0.4), incorporating SCMs such as silica fume (SF) and ground granulated blastfurnace slag (GGBS), and superplasticiser to enhance workability. However, such concretes are susceptible to autogenous shrinkage and microcracking induced by self-desiccation. Such cracks may partially negate the advantages of HPC by reducing its strength and durability through the provision of preferential pathways for the transport of water and deleterious species. Autogenous shrinkage is known to become significant at water/cement ratio of ≤ 0.42 [1], where all capillary water is consumed and the capillary pore structure becomes depercolated.

While there are many studies focusing on the nature of autogenous deformation [2-6] and possible mitigation methods [6-9], there are very few studies which examine the associated microcracking. Where studies are available, they involve mainly model composite samples using idealised elements as internal restraints [10, 11]. For example, Lura *et al.* [11] used model composites consisting of steel rods of different sizes cast within cement paste to study the formation of microcracks under autogenous conditions. They found that microcracks propagated in radial direction for 1 to 2 mm from the rod, ranging from 11 to 25 µm in width. Clearly, such characterisation is not representative of real concrete which is inherently multiphase, multiscale, time-dependent and three-dimensional. Additionally, autogenous shrinkage-induced microcracks are sensitive to external moisture and temperature, and therefore especially difficult to characterise without inadvertent modification [10]. This can be overcome with the use of non-destructive X-ray imaging, which provides 3D representations of microcracks with minimal disturbance to the sample [12, 13].

Despite the significance of autogenous shrinkage-induced microcracks, their actual effect on long-term transport properties remains unclear. While there are studies that have characterised the transport properties of low w/b cementitious systems containing SCMs [14-18] and shrinkage reducing admixture (SRA) [19, 20], none have linked them to autogenous shrinkage and related microcracking. A probable reason for this lies in the fact that it is practically difficult to de-couple the contribution of microcracks from those of gel and capillary porosity, and air voids which are inherently interconnected. Furthermore, transport measurements are critically dependent on the moisture state of concrete and pre-conditioning is required to empty accessible pores (including microcracks) to ensure meaningful measurements [15]. Previous studies [21, 22] have investigated the influence of drying-induced microcracking and related size effects on transport properties of conventional concretes. However, such microcracks occur mainly near the surface exposed to drying and as such are not comparable to those induced by autogenous shrinkage.

* Corresponding author. E-mail: hong.wong@imperial.ac.uk Telephone: +44 (0)20 7594 5956

This paper attempts to characterise autogenous shrinkage-induced microcracks and their influence on transport properties of concrete. A range of concretes with different binder types, w/b ratio, maximum size of aggregate and SRA, cured for up to ~3.6 years were investigated. Microcracks were characterised using laser scanning confocal microscopy (LSCM) and three-dimensional X-ray microtomography (X-ray μCT). Oxygen diffusivity and permeability, water sorptivity and accessible porosity were measured and correlated with observed microcracks. The aim was to establish the link between autogenous shrinkage and microcracking, and to what extent these influence mass transport. It is anticipated that this work would provide a better understanding of the significance of autogenous shrinkage on the long-term durability of concrete.

2 Experimental

2.1 Materials and mix proportions

Twenty-seven concrete mixes were prepared according to the proportions in Table 1. These were classified into three series according to binder type. Each series consists of 9 mixes with different w/b ratio (0.20, 0.25, 0.30, 0.35, 0.40 and 0.45), maximum size of aggregate (MSA: 5, 10, 20 mm) and a mix containing SRA to serve as reference. The mixes were designed to absolute volume. Ordinary Portland cement CEM I 52.5R, CEM I 52.5R with 9 wt.% replacement of SF, and pre-blended CEM III/B 42.5N containing 70% GGBS were used as binders. Their oxide composition, loss on ignition, specific gravity and fineness are shown in Table 2.

A polycarboxylate-based superplasticiser (Sika® ViscoCrete 20RM) was used to improve the workability of mixes with w/b ratios ≤ 0.35. A hydroxyl compound-based SRA (Sika® Control 40) was used to reduce shrinkage in the reference mixes. The amount of superplasticiser required to achieve good compaction was determined from trial mixes, while the amount of SRA was based on the manufacturer's recommended dosage (1 wt. % binder). Thames Valley sand with MSA of 5 mm and Thames Valley gravel with MSA of 5, 10 and 20 mm were used as fine and coarse aggregates respectively. Aggregate fraction was set to 68% vol. at fine-to-total aggregate mass ratio of 0.40 for all mixes. The aggregate particle size distributions are shown in Fig. 1. Their specific gravity, 24-h water absorption and moisture content are provided in Table 3. Tap water was used as batch water, adjusted to account for aggregate absorption.

2.2 Samples and curing

Cement and aggregates were dry-mixed in a 30-litre pan mixer for 30 s. Water was then added for further mixing of 3 min. Silica fume and superplasticiser were pre-mixed with batch water. 81 cylinders of 80 mm Ø × 300 mm were cast for linear deformation and transport measurements. These dimensions were chosen to achieve length/diameter ratio ≥ 3.5 and diameter/MSA ratio ≥ 4 to ensure good sampling volume and measurements [23]. The moulds were made of stiff tubes internally lined with polyethene to avoid leakage and to reduce friction. The two ends were wax sealed with plastic caps with a steel stud (5 mm Ø × 16.5 mm) half embedded in concrete. Three replicates were prepared for each mix. In addition, 24 discs of 95 mm Ø × 65 mm were cast in lidded plastic moulds for microcrack characterisation with laser scanning confocal microscopy (LSCM). Samples were vibrated in three layers until no significant release of air bubbles. All were compactable with no evidence of bleeding.

Samples were hermetically sealed to prevent moisture exchange, then laid horizontally and cured at 20 °C for 3.6 years in order to study the impact of microcracking on long-term transport properties. Periodic weighing showed mass loss of concrete of < 0.4% over time, indicating that the samples were effectively sealed and drying shrinkage was negligible. After curing, the discs were demoulded and a thin slice of 65 × 95 × 8 mm^3 was sectioned vertically with a diamond precision saw from the centre for LSCM. In addition, cylindrical cores of 30 mm Ø × 65 mm were diamond-cored from the SF-blended samples for 3D X-ray μCT observation. Our previous study [13] showed that autogenous shrinkage-induced microcracking was most severe at early ages and most microcrack characteristics became relatively stable from 7 d onwards. The cores for X-ray μCT were scanned as-is whereas the slices for LSCM were prepared as described in Section 2.5.

2.3 Linear deformation

A length comparator with a digital gauge of 0.001 mm accuracy was used for shrinkage measurement. Prior to each measurement, the device was calibrated with a 300 mm invar reference rod. The initial length (L_o) was taken when the samples had set (~6 h after casting for CEM I and SF systems; ~12 h for CEM III systems). The cylinders were carefully loaded onto the device with the end studs aligned with the gauge. Subsequent length readings (L) were taken daily for the first 2-3 weeks, then at weekly intervals. The linear strain was calculated as $(L - L_o) \div L_o \times 10^6$ (με). Three replicates were measured and averaged. Further details on the experimental set-up are available in [24].

2.4 Mass transport properties

The 80 mm Ø × 300 mm cylinders were sectioned from the centre using a diamond abrasive cutter to produce four replicate discs of 80 mm Ø × 50 mm for mass transport testing. The discs were conditioned at 50% RH, 20 °C in sealed environmental chambers until equilibrium (mass change ≤ 0.002% per day). The chambers contained saturated magnesium nitrate hexahydrate to maintain RH, soda lime to prevent carbonation and motorised fan for air circulation. Weight loss from drying was small because the samples had low w/b ratios and were sealed cured for 3.6 years prior to conditioning. Nevertheless, it is important to ensure homogenous moisture state across all samples for meaningful transport measurements [15].

O_2 diffusivity, O_2 permeability and water sorptivity were measured in sequence. O_2 diffusion was performed by exposing the opposite flat faces of the disc to O_2 and N_2 streams respectively at equal pressure. The sample was sealed with a silicone rubber ring at a small lateral confinement of 0.57 MPa in a steel cell to prevent side leakage without causing damage or crack closure [25]. The gases counter-diffused through the sample and the O_2 concentration in the outflow N_2 stream was monitored at steady state using a zirconia analyser. The O_2 concentration and flow rates were used to calculate the diffusion coefficient according to Fick's first law of diffusion.

O_2 permeation was conducted in a similar cell by subjecting one face of the disc to O_2 and measuring the outflow from the other face at steady state. Three gas pressures: 0.5, 1.5 and 2.5 bars were tested. At each pressure, the apparent permeability was calculated using Darcy's law for compressible fluids. Klinkenberg correction for gas slippage was then applied to determine the intrinsic permeability coefficient.

Water absorption was performed by placing the disc on two plastic strips in a tray containing water at depths of 2 to 3 mm from the wetted surface. The amount of water absorbed was measured periodically up to 3 weeks with an electronic balance of 0.01 g accuracy. The tray was covered to prevent drying of the sample and care was taken to avoid condensation forming/falling on the sample. The absorption per unit inflow area was plotted against square-root of time and sorptivity was determined from the slope of the regression line across nine readings taken in the first 24 h. In cases where absorption was extremely low, the regression line was extended to cover more readings. The R^2 value was ≥ 0.9 in all cases. Following water absorption, the discs were submerged in water under vacuum for 4 h and then left submerged until full saturation (< 7 d) to determine accessible porosity.

2.5 Imaging microcracks

Slices for LSCM were dried by sublimation using rapid freeze-drying to reduce the risk of additional drying induced damage [26, 27]. The slices were then impregnated with fluorescent epoxy to preserve the microcracks according to the procedures described in [28]. A low-viscosity epoxy resin (Struers EpoFix) doped with 0.05 wt.% fluorescein (Struers EpoDye) and thinned with 5 wt.% toluene was used. The samples were de-aired at -1 bar for 40 min before resin was introduced without breaking the vacuum. Following that, compressed air at 2.5 bars was applied for 2 h to increase impregnation. After the epoxy was fully cured, the samples were ground flat and polished with diamond at successively finer grits to 1 µm.

LSCM imaging was performed with a Leica TCS SP5. A 5× objective with a field of view of 3.10 × 3.10 mm^2 and a theoretical *xy* resolution of 1.30 µm was used. This is sufficient to resolve and characterise the microcracks. An argon laser of 488 nm (15% intensity) and a band pass filter of 500 to 600 nm were used for optimal excitation and detection of fluorescence. The pinhole was maintained at 1 Airy unit. The images were digitised to 2048 × 2048 pixels with a spacing of 1.514 µm. The detector sensitivity was adjusted to ensure optimal contrast. Automated tile imaging was performed with a motorised scanning stage (0.025 µm resolution) to capture the entire sample cross-section (65 × 95 mm^2). In total, 600 images (20 × 30 tiles with 10% overlapping) were acquired per sample.

The cores for X-ray µCT (SF-blended samples) were scanned with Metris X- Tek HMX ST 225. Despite its lower spatial resolution than LSCM, X-ray µCT provides 3D images of the microcracks for topological characterisation of connectivity and tortuosity [13]. The X-ray source was set to 220 kV and 200 µA, and a 0.5 mm thick copper filter was used to minimise beam-hardening effects. The source-sample-detector distances were set to 91.5 mm and 1088 mm respectively. The rotation step was set to 0.1146° and a total of 3142 projections were acquired. The exposure time was 1.25 s per frame and the total imaging time was ~1 h per sample. Image reconstruction was performed with centre shift and beam hardening corrections applied. The reconstructed image volumes were digitised to 2011 × 2011 × 2011 voxels at 15.5 µm voxel size.

2.6 Image analysis

The image tiles collected with LSCM were stitched based on phase correlation [29] in Fiji [30]. Solid phases such as aggregates and cement paste appear dark whereas pores, air voids and microcracks filled with fluorescent epoxy

appear green. Microcracks can be distinguished from other features based on their elongated morphology, high brightness and well-defined boundaries. A local thresholding approach was adopted to segment the microcracks. Amongst several methods tested (e.g. Bernsen [31], Phansalkar [32] and Niblack [33]), Sauvola's method [34] was found to be the most satisfactory and produced segmented microcracks that matched the original image. This method calculates threshold based on the mean grey level and standard deviation at a local domain set to 20 pixels. Other segmented features such as air voids, pores or noise (Fig. 2b) were removed via filtering and morphological operations in Avizo® Fire. Further details can be found in [24].

The 3D X-ray μCT images were segmented following the procedures described in [13]. In brief, the image was median-filtered and segmented using the Overflow method [35]. Following that, a series of filtering and morphological operations were applied to separate microcracks from other connected phases. These involved removal of aggregates with low grey levels overlapping with those of microcracks and air voids, removal of air voids based on shape factor and volume, and preservation and clean-up of remaining microcracks.

Eight parameters were quantified. These are summarised in Table 4 and detailed in [13, 36-42]. Measurements were performed using either BoneJ (v.1.40) in Fiji or Avizo® Fire. Connectivity and tortuosity were measured in 3D. The segmented microcracks were skeletonised using medial-axis thinning algorithm for measuring crack length and density. The microcracks were labelled based on 26-neighbourhood to identify every voxel that touches one of the faces, edges or corners of the largest percolated network for calculating connectivity.

3 Results

3.1 Autogenous shrinkage

Fig. 2 shows the measured linear deformation. All samples without SRA experienced the highest rate of shrinkage in the first 14 d which then gradually decreased over time, consistent with other studies [13, 43, 44]. Total shrinkage ranged between 100 and 350 με. GGBS and SF increased total shrinkage by an average factor of ~1.9 and ~1.3 respectively relative to CEM I only systems. On average, over 82% of the total shrinkage occurred in the first two weeks for the GGBS blended concrete, compared to 65% for SF blended and 48% for the CEM I only concretes. In contrast, samples with SRA showed a slight expansion (< 60 με) in the first 3 weeks, followed by gradual shrinkage. The initial expansion is due to increased oversaturation and crystallisation of portlandite [45-47]. SRA was clearly effective in reducing the rate and magnitude of shrinkage by a factor of 4 to 5. Mixes containing SCMs showed the largest reduction.

As expected, mixes with low w/b ratio experienced higher autogenous shrinkage due to less water available and hence greater self-desiccation. A noticeable increment in shrinkage was observed between w/b 0.45 to 0.40, especially for blended systems. This corresponds to the w/b ratio at which the amount of available water is insufficient for complete hydration. It is interesting to note that shrinkage increased with maximum aggregate size (MSA) irrespective of binder type (Fig. 2d). This is because a larger particle size at constant aggregate content reduces the total aggregate surface area that bonds with cement paste and hence the amount of restraint to shrinkage.

3.2 Transport properties

Fig. 3 presents the average transport properties plotted against total autogenous shrinkage. The transport data spanned between one and three orders of magnitude, ranging from 1.09 to 4.89 × 10^{-9} m^2/s for diffusivity, 0.23 to 71.1 × 10^{-18} m^2 for permeability and 1.24 to 23.5 $g/m^2 \cdot min^{0.5}$ for sorptivity. It is worth noting that these are significantly lower than the values reported in our previous studies [21, 48] consistent with the fact that the concretes tested in this study have smaller w/b ratios and longer curing age.

As expected, lowering the w/b ratio and the presence of SCMs decreased long-term mass transport. Overall, concretes with GGBS gave the lowest mass transport properties. Relative to CEM I concretes, GGBS decreased mass transport by an average of 33%, 27% and 26% for diffusivity, permeability and sorptivity respectively, after the 3.6 years of sealed curing. The corresponding values for SF were 26%, 13% and 16%. SCMs had a greater effect on mixes at high w/b ratio.

When comparing mixes at the same w/b ratio (0.3) and binder type, it is clear that the use of SRA decreased transport properties substantially in all cases. The reduction was at least a factor of 2 to over 45, and the most pronounced reduction occurred for permeability. Therefore, autogenous shrinkage has a significant influence on mass transport properties. It should however be pointed out that SRA can increase the viscosity and decrease the surface tension of pore solution and this may also contribute to reduced water sorption [49].

Fig. 4 shows strong positive correlations between transport properties and accessible porosity irrespective of mix composition (w/b ratio, binder type, SRA and MSA). It should be noted here that the measured porosity is the sum of pores, air voids and cracks that are accessible to transport. Therefore, the strong correlations suggest that both pores

and cracks contribute to transport. However, the correlation for permeability showed greater scatter compared to diffusivity and sorptivity. This is due to the fact that pressure-induced flow occurs preferentially through paths of least resistance and hence, permeability is highly sensitive to presence of interconnected microcracks [50].

3.3 Maximum aggregate size

Table 5 presents the mass transport properties and accessible porosity of concretes at w/b 0.30 with different maximum aggregate size (MSA) to examine size effects. Given that all systems shown in Table 5 had the same w/b ratio, aggregate volume and curing age, their accessible porosity and transport properties were expected to be invariant to MSA. However, this was not the case. The results consistently showed that transport properties and accessible porosity increased with increasing MSA. The size effect was most pronounced with blended systems. Diffusivity and sorptivity increased by up to a factor of 2 to 3, but permeability increased by over a factor of 30 to 700. This can only be attributed to additional microcracks (rather than capillary or gel porosity) that formed in systems containing larger coarse aggregate particles, consistent with the increase in autogenous shrinkage shown in Fig. 2d.

3.4 Microstructure

Fig. 5 presents example LSCM images of the silica fume-blended samples. Mixes at lower w/b ratio showed decreased fluorescence intensity due to reduced capillary porosity, but a greater amount of microcracking. The microcracks appear interconnected and distributed across the entire cross-section. They occur either at aggregate-paste interface (bond cracks) or through the cement paste (matrix cracks, marked by arrows), with tendency to propagate through air voids. The notable presence of air voids which can be as high as ~2% at low w/b ratio was to be expected due to difficulties in achieving full compaction [13, 51]. At the same w/b ratio, the presence of SRA reduced microcracking significantly.

Fig. 6 shows example 3D views of the segmented microcracks obtained with X-ray μCT. The microcracks are shaded to indicate local thickness (width). The microcracks appear spatially distributed throughout the of 30 Ø × 65 mm cores. The amount, length and connectivity of microcracks increased at lower w/b ratio. Many envelopes of bond cracks are visible, indicating that the orientation of microcracks is dependent on that of aggregates.

3.5 Quantitative analysis of microcracks

Table 6 presents the measured microcrack characteristics. Cumulative distribution of width and length of microcracks are shown in Fig. 7. The average widths ranged from ~ 15 to 100 μm. The results show that volume fraction, average width and length, density and connectivity of the microcracks increased with decreasing w/b ratio. In contrast, tortuosity decreased while specific surface area and degree of anisotropy remained relatively constant. Overall, the microcracks are relatively isotropic due to the random orientation of aggregate particles independent of w/b ratio. As expected, the number of cracks decreased with increasing microcrack volume fraction and connectivity.

Comparing mixes of the same w/b ratio, it is evident that the presence of SCMs increased the amount of microcracking. The effect of GGBS was most pronounced, in line with the measured autogenous shrinkage (Fig. 2). However, the presence of SRA decreased microcracking significantly. For example, the volume fraction, average length and density of microcracks decreased by up to 9×, 2× and 5× respectively. The specific surface area increased by up to 13×, possibly due to pore refinement [52].

The effect of MSA on microcracking is shown in Table 7. The volume fraction, width and length of microcracks increased with increasing MSA. For example, the volume fraction and average width of microcracks increased by 6× and 3× respectively when MSA increased from 5 to 20 mm. This is consistent with the increase in autogenous shrinkage (Fig. 2d) and confirms that the observed size effects in mass transport (Table 5) are linked to microcracks. Specific surface area and degree of anisotropy remained relatively constant.

3.6 Correlations between microcracks, autogenous shrinkage and mass transport

Fig. 8 plots the correlations between microcrack volume fraction, autogenous shrinkage and accessible porosity for all samples. It is clear that the amount of microcracking increased with autogenous shrinkage (Fig. 8a), but decreased at higher accessible porosity (w/b ratio) and with the presence of SRA, irrespective of binder type (Fig. 8b). This shows that the observed microcracking was induced by autogenous shrinkage and that it had greater severity in denser matrix, consistent with previous studies on drying shrinkage [21, 53]. At the same w/b ratio, microcracking increased with MSA (Fig. 8c). This confirms that the size effects discussed in Section 3.3 are indeed caused by additional microcracking that formed in concretes containing larger aggregate particles.

4 Discussion

4.1 Other factors that may contribute to microcracking

Sample preparation for microscopy may cause artificial microcracking, particularly during the initial sectioning and freeze-drying processes. However, the possibility of damage during grinding and polishing is reduced by epoxy impregnation. Furthermore, any new cracks that form after epoxy impregnation would not fluoresce and hence are not visible under LSCM. To assess the potential damage, a reference concrete was prepared with CEM I 52.5R at 0.50 w/c ratio, 10 mm MSA and cured for 14 days in saturated lime solution. The concrete was then sectioned, freeze-dried, epoxy impregnated, ground and polished, and characterised using LSCM following the same procedures described in Sections 2.5 and 2.6. The high w/c ratio and short wet curing would prevent autogenous shrinkage, but increase the risk of mechanical damage. Thus, the reference was likely to overestimate the extent of sample preparation damage.

The analysis showed that the reference concrete had microcracks, but these were sparsely distributed and much less severe compared to the sealed cured samples. The microcrack volume fraction and density were only 0.07% and 0.06 mm/mm^2 respectively, and 95% of the microcracks had widths below 20 µm (average 11.5 µm). These are small compared to the values reported in Tables 6 and 7, and Fig. 7. Nevertheless, the potential damage induced by sample preparation is not negligible and this should be kept in mind when interpreting microscopy data. In any case, all samples were subjected to the same preparation to allow a fair comparison.

4.2 Comparison between autogenous shrinkage and drying shrinkage microcracks

It would be interesting to compare autogenous shrinkage-induced microcracks with those induced by drying shrinkage since concrete structures can be exposed to both conditions. Previous studies [21, 22, 48] have characterised microcracking in pastes, mortars and concretes with and without SCMs (SF, GGBS, PFA), when subjected to various drying severity from gentle stepwise drying at 21°C/93%→3% RH to more extreme drying at 21°C/55% RH, 21°C/33% RH, 21°C/0% RH, 50°C/7% RH or 105°C. The results collectively showed that drying-induced microcracks occur near the exposed surface only and propagate into depths of several mm. The crack width, length and density increased with drying severity. However, the majority of the cracks (over 80%) had widths less than 10 µm and lengths shorter than 100 µm, even in the most severe drying conditions. The microcracks contribute only 0.1 to 1.3% of the total accessible porosity. These values are much smaller compared to microcracks induced by autogenous shrinkage (cf. Tables 6 and 7, Figs. 7 and 8). Furthermore, autogenous-shrinkage induced microcracks are well-distributed and interconnected throughout the entire sample volume (Figs. 5 and 6).

4.3 Size effects on shrinkage, microcracking and mass transport properties

Increasing the aggregate particle size consistently led to an increase in autogenous shrinkage, microcracking, accessible porosity and mass transport, especially permeability. This is similar to the size effects observed in cementitious materials subjected to drying shrinkage [21, 54], but it is worth noting that the impact on mass transport found in this study is much larger than that reported in Wu et al. 2014 [ref] on 28-day CEM I mortars and concretes at 0.5 w/c ratio. This is in line with the results showing that autogenous shrinkage causes a more severe and percolated microcracking compared to drying shrinkage. Furthermore, the effect of microcracking on mass transport is more pronounced in systems with dense matrix (low w/b ratio, prolonged curing) compared to a more porous matrix, as shown in three-dimensional flow simulations [50]. Microcracks become the predominant flow paths in very dense matrix containing little or no capillary porosity.

It is worth pointing out that the observed size effects cannot be attributed to percolation of the so-called porous interface transition zone (ITZ) between aggregate and cement paste. Firstly, the use of SCMs, low w/b ratio and prolonged curing mean that the samples tested in this study would have very dense ITZs, as seen in the microstructure (Fig. 5). Secondly, increasing MSA at constant aggregate content equates to fewer aggregate particles, smaller surface area and thus lower interface regions per sample volume. Thirdly, the separating distance between neighbouring ITZs increases at larger MSA. All of these factors cannot explain why transport increases with MSA (cf. Table 5 and Fig. 8c), therefore ITZ is not the main influencing factor. However, microcracking could increase the connectivity of the ITZ, thereby exacerbating its effect on transport.

4.4 Significance of autogenous shrinkage on mass transport properties

It is well-known that low w/b ratio systems containing SCMs such as GGBS and SF have dense microstructure and low mass transport properties. This is despite the fact that they experience high autogenous shrinkage (e.g. [43, 55, 56]). For example, three-dimensional microscopy showed that GGBS and SF refine capillary pore structure, reduce percolation connectivity and increase diffusion tortuosity [18]. However, self-desiccation decreases internal humidity, causing the paste matrix to shrink over time. The consumption of portlandite by pozzolanic reaction of the SCMs is also

believed to induce additional shrinkage due to the removal of micro-restraints in the paste matrix [6]. This shrinkage can lead to microcracking that increases long-term mass transport and partly offsets the beneficial effect of pore refinement.

Real concrete structures are rarely maintained under strict autogenous conditions. They are often exposed to cyclic drying and wetting which can induce further dimensional changes and microcracking. The thermal effects from early cement hydration and SCM reactions can also induce thermal expansion and contraction which in turn affect the magnitude and rate of autogenous shrinkage [23]. This is especially significant in large concrete structures where internal heat cannot be dissipated and may therefore exacerbate microcracking.

However, very few studies have examined the nature of the associated microcracking and its impact on long-term performance. This is due to the difficulties in characterising the microcracks in three-dimensions and isolating their effect from those of capillary and gel pores, and air voids that are inherently interconnected. The data from this study shows that after 3.6 years of sealed curing, blended concretes at low w/b ratio continue to show the lowest mass transport properties, despite experiencing the highest amount of autogenous shrinkage-induced microcracking. Nevertheless, the microcracking can be mitigated to a large extent by using small aggregate particle sizes and by incorporating shrinkage reducing admixture. Our data shows that such measures can further decrease long-term diffusivity and sorptivity by a factor of 2 to 3, and decrease permeability by over a factor of 30 to 700.

5 Conclusions

This study examined the influence of autogenous shrinkage on microcracking and long-term mass transport properties of concretes containing supplementary cementitious materials. Twenty-seven concretes with different binder types (CEM I, CEM I with 9% silica fume replacement, CEM III containing 70% GGBS), w/b ratio (0.20 to 0.45), maximum aggregate size (MSA: 5, 10, 20 mm) and shrinkage reducing admixture (SRA) were prepared and subjected to sealed curing for up to ~3.6 years. Oxygen diffusivity, permeability and water sorptivity were tested and the results correlated to microcrack characteristics obtained using laser scanning confocal microscopy and three-dimensional X-ray microtomography. The key findings are:

a. Total autogenous shrinkage ranged between 100 and 350 με. The highest shrinkage occurred in concretes with low w/b ratio containing SCMs and larger aggregate particles. The presence of silica fume and GGBS increased autogenous shrinkage by a factor of ~1.3 and ~1.9 respectively relative to the CEM I systems. SRA decreased the rate and magnitude of shrinkage by a factor of 4 to 5, with blended mixes showing the largest reduction.

b. Autogenous shrinkage induces microcracks that are interconnected and distributed across the sample volume with average widths ranging from ~ 15 to 100 μm. The volume fraction, width and length, density and connectivity of the microcracks increased with increase in shrinkage. In contrast, tortuosity decreased while the specific surface area and degree of anisotropy remained relatively constant. Mixes containing SCMs and large aggregate particles showed the most severe microcracking. The use of SRA decreased microcracking, consistent with the reduction in shrinkage.

c. In comparison with drying-induced microcracks, autogenous shrinkage-induced microcracks are larger in size, more densely distributed and interconnected. They occur throughout the sample whereas drying-induced microcracks occur near the first several mm of the exposed surface only.

d. Increasing the aggregate particle size consistently led to an increase in autogenous shrinkage, accessible porosity and mass transport, especially permeability. Transport properties increased with MSA due to the increase in microcracking and the effect was most pronounced with blended systems. This is similar to the size effects observed in cementitious materials subjected to drying shrinkage.

e. Relative to CEM I concretes, GGBS decreased mass transport by an average of 33%, 27% and 26% for diffusivity, permeability and sorptivity respectively. The corresponding values for SF were 26%, 13% and 16%. SCMs had a greater effect on concretes at high w/b ratio.

f. Blended concretes at low w/b ratio show the lowest long-term mass transport properties, despite having the highest autogenous shrinkage and microcracking. However, further improvements in durability of such concrete is possible by removing these microcracks, either by using shrinkage reducing admixture or small aggregate particle size. We estimate that such measures can further decrease diffusivity and sorptivity by a factor of 2 to 3, and decrease permeability by over a factor of 30 to 700.

Acknowledgements

M.J. Mac acknowledges the funding from the European Union Seventh Framework Programme under grant agreement 264448. We thank Mr Andrew Morris for his help with the laboratory work. The research leading to this publication benefitted from EPSRC funding under grant No. EP/R010161/1 and from support from the UKCRIC Coordination Node, EPSRC grant number EP/R017727/1, which funds UKCRIC's ongoing coordination.

References

[1] P.C. Aïtcin, Phenomenology of cement hydration, in: P.-C. Aïtcin, R.J. Flatt (Eds.) Science and Technology of Concrete Admixtures, Woodhead Publishing2016, pp. 15-25.
[2] E.-i. Tazawa, S. Miyazawa, Influence of cement and admixture on autogenous shrinkage of cement paste, Cement and Concrete Research, 25 (1995) 281-287.
[3] S.-i. Igarashi, A. Bentur, K. Kovler, Autogenous shrinkage and induced restraining stresses in high-strength concretes, Cement and Concrete Research, 30 (2000) 1701-1707.
[4] O.M. Jensen, P.F. Hansen, Autogenous deformation and RH-change in perspective, Cement and Concrete Research, 31 (2001) 1859-1865.
[5] A. Bentur, Report 25: Early Age Cracking in Cementitious Systems-Report of RILEM Technical committee TC 181-EAS: Early age cracking shrinkage induced stresses and cracking in cementitious systems, RILEM publications, 2003.
[6] P. Lura, Autogenous deformation and internal curing of concrete, PhD Thesis, TU Delft, Delft, 2003.
[7] O.M. Jensen, P. Lura, Techniques and materials for internal water curing of concrete, Materials and Structures, 39 (2006) 817-825.
[8] K. Kovler, O. Jensen, Internal curing of concrete, state-of-the-art Report of RILEM Technical Committee 196-ICC, RILEM Report, 41 (2007).
[9] D.P. Bentz, M.A. Peltz, Reducing thermal and autogenous shrinkage contributions to early-age cracking, ACI Materials Journal, 105 (2008) 414.
[10] P. Lura, J. Weiss, O.M. Jensen, Detection and analysis of microcracks in high-performance cementitious materials, Springer Berlin Heidelberg, Berlin, Heidelberg, 2007, pp. 607-614.
[11] P. Lura, O.M. Jensen, J. Weiss, Cracking in cement paste induced by autogenous shrinkage, Materials and Structures, 42 (2009) 1089-1099.
[12] M.J. Mac, M.H.N. Yio, G. Desbois, I. Casanova, H.S. Wong, N.R. Buenfeld, 3D imaging techniques for characterising microcracks in cement-based materials, Cement and Concrete Research, 140 (2021) 106309.
[13] M.J. Mac, M.H.N. Yio, H.S. Wong, N.R. Buenfeld, Analysis of autogenous shrinkage-induced microcracks in concrete from 3D images, Cement and Concrete Research, 144 (2021) 106416.
[14] L.O. Nilsson, Long-term moisture transport in high performance concrete, Materials and Structures, 35 (2002) 641-649.
[15] H.S. Wong, N.R. Buenfeld, J. Hill, A.W. Harris, Mass transport properties of mature wasteform grouts, Advances in Cement Research, 19 (2007) 35-46.
[16] E. Ghafari, H. Costa, E. Júlio, A. Portugal, L. Durães, The effect of nanosilica addition on flowability, strength and transport properties of ultra high performance concrete, Materials & Design, 59 (2014) 1-9.
[17] W. Piasta, B. Zarzycki, The effect of cement paste volume and w/c ratio on shrinkage strain, water absorption and compressive strength of high performance concrete, Construction and Building Materials, 140 (2017) 395-402.
[18] M.H.N. Yio, H.S. Wong, N.R. Buenfeld, 3D pore structure and mass transport properties of blended cementitious materials, Cement and Concrete Research, 117 (2019) 23-37.
[19] A.B. Ribeiro, A. Gonçalves, A. Carrajola, Effect of shrinkage reduction admixtures on the pore structure properties of mortars, Materials and Structures, 39 (2006) 179-187.
[20] W. Zuo, P. Feng, P. Zhong, Q. Tian, J. Liu, W. She, Effects of a novel polymer-type shrinkage-reducing admixture on early age microstructure evolution and transport properties of cement pastes, Cement and Concrete Composites, 95 (2019) 33-41.
[21] Z. Wu, H.S. Wong, N.R. Buenfeld, Influence of drying-induced microcracking and related size effects on mass transport properties of concrete, Cement and Concrete Research, 68 (2015) 35-48.
[22] Z. Wu, H.S. Wong, C. Chen, N.R. Buenfeld, Anomalous water absorption in cement-based materials caused by drying shrinkage induced microcracks, Cement and Concrete Research, 115 (2019) 90-104.
[23] E.-i. Tazawa, Autogenous shrinkage of concrete, CRC Press, London, 1999.
[24] M.J. Mac, 3D Characterisation of microcracks in concrete, PhD Thesis, Imperial College London, London, 2019.
[25] Z. Wu, H.S. Wong, N.R. Buenfeld, Effect of confining pressure and microcracks on mass transport properties of concrete, Advances in Applied Ceramics, 113 (2014) 485-495.

[26] N.C. Collier, J.H. Sharp, N.B. Milestone, J. Hill, I.H. Godfrey, The influence of water removal techniques on the composition and microstructure of hardened cement pastes, Cement and Concrete Research, 38 (2008) 737-744.
[27] J. Zhang, G.W. Scherer, Comparison of methods for arresting hydration of cement, Cement and Concrete Research, 41 (2011) 1024-1036.
[28] H.S. Wong, N.R. Buenfeld, Patch microstructure in cement-based materials: Fact or artefact?, Cement and Concrete Research, 36 (2006) 990-997.
[29] S. Preibisch, S. Saalfeld, P. Tomancak, Globally optimal stitching of tiled 3D microscopic image acquisitions, Bioinformatics, 25 (2009) 1463-1465.
[30] J. Schindelin, I. Arganda-Carreras, E. Frise, V. Kaynig, M. Longair, T. Pietzsch, S. Preibisch, C. Rueden, S. Saalfeld, B. Schmid, J.-Y. Tinevez, D.J. White, V. Hartenstein, K. Eliceiri, P. Tomancak, A. Cardona, Fiji: an open-source platform for biological-image analysis, Nat Meth, 9 (2012) 676-682.
[31] J. Bernsen, Dynamic thresholding of gray-level images, Proc. Eighth Int'l conf. Pattern Recognition, Paris, 1986, 1986.
[32] N. Phansalkar, S. More, A. Sabale, M. Joshi, Adaptive local thresholding for detection of nuclei in diversity stained cytology images, 2011 International Conference on Communications and Signal Processing, 2011, pp. 218-220.
[33] W. Niblack, An introduction to digital image processing, Strandberg Publishing Company, Birkerød, 1985.
[34] J. Sauvola, M. Pietikäinen, Adaptive document image binarization, Pattern Recognition, 33 (2000) 225-236.
[35] H.S. Wong, M.K. Head, N.R. Buenfeld, Pore segmentation of cement-based materials from backscattered electron images, Cement and Concrete Research, 36 (2006) 1083-1090.
[36] M.W. Crofton, J. Sylvester, On the Theory of Local Probability, Applied to Straight Lines Drawn at Random in a Plane: The Methods Used Being Also Extenden to the Proof of Certain New Theorems in the Integral Calculus, 1868.
[37] T.P. Harrigan, R.W. Mann, Characterization of microstructural anisotropy in orthotropic materials using a second rank tensor, Journal of Materials Science, 19 (1984) 761-767.
[38] A. Odgaard, Three-dimensional methods for quantification of cancellous bone architecture, Bone, 20 (1997) 315-328.
[39] R. Dougherty, K.H. Kunzelmann, Computing Local Thickness of 3D Structures with ImageJ, Microscopy and Microanalysis, 13 (2007) 1678-1679.
[40] T. Hildebrand, P. Rüegsegger, A new method for the model-independent assessment of thickness in three-dimensional images, Journal of Microscopy, 185 (1997) 67-75.
[41] T.C. Lee, R.L. Kashyap, C.N. Chu, Building skeleton models via 3-D medial surface axis thinning algorithms, CVGIP: Graphical Models and Image Processing, 56 (1994) 462-478.
[42] S.J. Cooper, D.S. Eastwood, J. Gelb, G. Damblanc, D.J.L. Brett, R.S. Bradley, P.J. Withers, P.D. Lee, A.J. Marquis, N.P. Brandon, P.R. Shearing, Image based modelling of microstructural heterogeneity in LiFePO4 electrodes for Li-ion batteries, Journal of Power Sources, 247 (2014) 1033-1039.
[43] M.H. Zhang, C.T. Tam, M.P. Leow, Effect of water-to-cementitious materials ratio and silica fume on the autogenous shrinkage of concrete, Cement and Concrete Research, 33 (2003) 1687-1694.
[44] C. Jiang, Y. Yang, Y. Wang, Y. Zhou, C. Ma, Autogenous shrinkage of high performance concrete containing mineral admixtures under different curing temperatures, Construction and Building Materials, 61 (2014) 260-269.
[45] G. Sant, B. Lothenbach, P. Juilland, G. Le Saout, J. Weiss, K. Scrivener, The origin of early age expansions induced in cementitious materials containing shrinkage reducing admixtures, Cement and Concrete Research, 41 (2011) 218-229.
[46] M. Collepardi, A. Borsoi, S. Collepardi, J.J. Ogoumah Olagot, R. Troli, Effects of shrinkage reducing admixture in shrinkage compensating concrete under non-wet curing conditions, Cement and Concrete Composites, 27 (2005) 704-708.
[47] J. Weiss, P. Lura, F. Rajabipour, G. Sant, Performance of shrinkage-reducing admixtures at different humidities and at early ages, ACI Materials Journal, 105 (2008) 478.
[48] Z. Wu, H.S. Wong, N.R. Buenfeld, Transport properties of concrete after drying-wetting regimes to elucidate the effects of moisture content, hysteresis and microcracking, Cement and Concrete Research, 98 (2017) 136-154.
[49] C. Qiao, W. Ni, J. Weiss, Transport due to Diffusion, Drying, and Wicking in Concrete Containing a Shrinkage-Reducing Admixture, Journal of Materials in Civil Engineering, 29 (2017) 04017146.
[50] S.D. Abyaneh, H.S. Wong, N.R. Buenfeld, Simulating the effect of microcracks on the diffusivity and permeability of concrete using a three-dimensional model, Computational Materials Science, 119 (2016) 130-143.
[51] H.S. Wong, A.M. Pappas, R.W. Zimmerman, N.R. Buenfeld, Effect of entrained air voids on the microstructure and mass transport properties of concrete, Cement and Concrete Research, 41 (2011) 1067-1077.
[52] W. Zhang, Y. Hama, S.H. Na, Drying shrinkage and microstructure characteristics of mortar incorporating ground granulated blast furnace slag and shrinkage reducing admixture, Construction and Building Materials, 93 (2015) 267-277.

461 [53] H.S. Wong, M. Zobel, N.R. Buenfeld, R.W. Zimmerman, Influence of the interfacial transition zone and
462 microcracking on the diffusivity, permeability and sorptivity of cement-based materials after drying, Magazine of
463 Concrete Research, 61 (2009) 571-589.
464 [54] P. Grassl, H.S. Wong, N.R. Buenfeld, Influence of aggregate size and volume fraction on shrinkage induced micro-
465 cracking of concrete and mortar, Cement and Concrete Research, 40 (2010) 85-93.
466 [55] Y. Yang, R. Sato, K. Kawai, Autogenous shrinkage of high-strength concrete containing silica fume under drying at
467 early ages, Cement and Concrete Research, 35 (2005) 449-456.
468 [56] V. Baroghel-Bouny, P. Mounanga, A. Khelidj, A. Loukili, N. Rafaï, Autogenous deformations of cement pastes: Part
469 II. W/C effects, micro–macro correlations, and threshold values, Cement and Concrete Research, 36 (2006) 123-136.

470

471

Effect of autogenous shrinkage on microcracking and mass transport properties of concrete containing supplementary cementitious materials

M.H.N. Yio, M.J. Mac, Y.X. Yeow, H.S. Wong*, N.R. Buenfeld

Centre for Infrastructure Materials, Department of Civil and Environmental Engineering, Imperial College London, SW7 2AZ, United Kingdom

Table 1 Mix proportion of tested concretes.

Mix ID*	CEM I (kg/m³)	SF (kg/m³)	GGBS (kg/m³)	Water (kg/m³)	w/b (-)	MSA (mm)	Sand (kg/m³)	Gravel (kg/m³)	SP (kg/m³)	SRA (kg/m³)
CEM I										
0.20-C	586	-	-	117	0.20	10	718	1077	12	-
0.25-C	542	-	-	136	0.25	10	718	1077	8	-
0.30-C	503	-	-	151	0.30	10	718	1077	5	-
0.35-C	470	-	-	165	0.35	10	718	1077	2	-
0.40-C	441	-	-	176	0.40	10	718	1077	-	-
0.45-C	413	-	-	186	0.45	10	718	1077	-	-
0.30-C-5	503	-	-	151	0.30	5	702	1053	5	-
0.30-C-20	503	-	-	151	0.30	20	724	1086	5	-
0.30-C-SRA	495	-	-	149	0.30	10	718	1077	5	5
CEM I + 9% SF										
0.20-SF	534	53	-	117	0.20	10	718	1077	12	-
0.25-SF	485	48	-	133	0.25	10	718	1077	8	-
0.30-SF	451	45	-	149	0.30	10	718	1077	5	-
0.35-SF	422	42	-	162	0.35	10	718	1077	3	-
0.40-SF	396	39	-	174	0.40	10	718	1077	-	-
0.45-SF	371	37	-	183	0.45	10	718	1077	-	-
0.30-SF-5	451	45	-	149	0.30	5	702	1053	5	-
0.30-SF-20	451	45	-	149	0.30	20	724	1086	5	-
0.30-SF-SRA	444	44	-	146	0.30	10	718	1077	5	5
CEM III (70% GGBS)										
0.20-GGBS	170	-	397	113	0.20	10	718	1077	11	-
0.25-GGBS	158	-	368	132	0.25	10	718	1077	8	-
0.30-GGBS	147	-	342	147	0.30	10	718	1077	5	-
0.35-GGBS	137	-	321	160	0.35	10	718	1077	2	-
0.40-GGBS	129	-	301	172	0.40	10	718	1077	-	-
0.45-GGBS	121	-	282	181	0.45	10	718	1077	-	-
0.30-GGBS-5	147	-	342	147	0.30	5	702	1053	5	-
0.30-GGBS-20	147	-	342	147	0.30	20	724	1086	5	-
0.30-GGBS-SRA	145	-	337	145	0.30	10	718	1077	5	5

*C = CEM I; SF = silica fume; GGBS = ground granulated blastfurnace slag; SRA = shrinkage reducing admixture, MSA = maximum size of aggregate; SP = superplasticiser

* Corresponding author. E-mail: hong.wong@imperial.ac.uk Telephone: +44 (0)20 7594 5956

476 **Table 2 Oxide composition and physical properties of binders.**

Binder	Oxide composition (%)									Specific gravity (-)	Fineness (cm^2/g)	Loss on ignition (%)
	CaO	SiO_2	Al_2O_3	Fe_2O_3	MgO	Na_2O	K_2O	SO_3	Cl-			
CEM I 52.5 R	63.4	20.8	5.4	2.4	1.5	0.3	0.7	2.9	<0.1	3.06	2910	2.10
CEM III/B 42.5 N	48.0	29.2	8.9	1.2	4.8	0.2	0.6	2.6	0.1	2.90	4635	1.40
Silica fume	0.15	98.7	0.31	0.02	0.04	0.09	0.30	-	-	2.30	-	0.47

477

478

479 **Table 3 Properties of aggregates.**

Aggregate type	MSA (mm)	Specific gravity (-)	24-hr absorption (%)	Moisture content (%)
Sand	5	2.56	0.80	0.20
Gravel	5	2.60	0.79	0.50
	10	2.70	0.76	0.45
	20	2.74	0.72	0.40

480

481

482 **Table 4 Methods for quantifying microcracks.**

Parameter	Software	Method	Definition
Volume fraction	Fiji (BoneJ)	Pixel counting	Total area of microcracks ÷ image area
Specific surface area (SSA)	Avizo® Fire	Line-object intercept to compute Crofton perimeter [36]	Total Crofton perimeter ÷ total area of microcracks
Degree of anisotropy (DA)	Fiji (BoneJ)	Mean intercept length (MIL) [37,38]	DA = 1 – [minimum eigenvalue ÷ maximum eigenvalue of MIL vector cloud]; 0 < DA < 1 (0: isotropic, 1 = anisotropic)
Width	Fiji (BoneJ)	Thickness computing [39,40]	Area based local size of microcracks computed by fitting the largest circle to every point in the microcracks.
Length	Fiji (BoneJ)	Dendritic length via medial surface axis thinning [41]	Area ÷ pixel side length of individual skeletonised microcrack
Density	Fiji (BoneJ)	Dendritic density via medial surface axis thinning [41]	Total dendritic length of skeletonised microcracks ÷ image area
Connectivity	Avizo® Fire	Labelling	Volume of largest connected microcrack ÷ total volume of microcracks
Tortuosity	Avizo® Fire	Centroid path computing [42]	Total path length through centroids of microcracks on each image plane ÷ straight distance between two end planes along *x*, *y* or *z* axis

483

484

485

486

Table 5 Effect of maximum aggregate size (MSA: 5, 10, 20 mm) and binder type on transport properties and accessible porosity of 0.30 w/b concretes after 3.6 years sealed curing. Numbers in parentheses represent ± one standard error.

MSA	O^2 diffusivity ($\times 10^{-9}$ m^2/s)			O^2 permeability ($\times 10^{-18}$ m^2)			Water sorptivity ($g/m^2min^{0.5}$)			Accessible porosity (%)		
	C	SF	GGBS	C	SF	GGBS	C	SF	GGBS	C	SF	GGBS
5	1.91 (0.39)	1.10 (0.09)	1.09 (0.12)	0.23 (0.01)	< 0.1	< 0.1	10.1 (4.32)	6.12 (0.04)	5.24 (0.12)	2.37 (0.52)	1.30 (0.02)	1.52 (0.04)
10	2.86 (0.18)	2.16 (0.04)	1.73 (0.17)	4.52 (0.84)	0.50 (0.19)	0.44 (0.23)	9.10 (0.73)	7.58 (0.25)	5.60 (0.13)	4.30 (0.60)	3.46 (0.12)	1.52 (0.10)
20	2.93 (0.26)	3.56 (0.19)	3.10 (0.60)	7.74 (2.87)	71.1 (13.9)	22.4 (5.74)	12.6 (1.65)	16.3 (2.36)	13.1 (0.71)	5.68 (0.76)	5.91 (0.49)	5.27 (0.80)

***** C = CEM I, SF = silica fume, S = slag

Table 6 Effect of w/b ratio and binder type on the characteristics of autogenous shrinkage induced microcracks in concretes with MSA 10 mm.

w/b	Vol. fraction (%)			Spec. surface (mm^{-1})			Density (mm/mm^2)			Degree of anisotropy (-)			Connectivity (-) SF	Tortuosity (-) SF		
	C	SF	GGBS	C	SF	GGBS	C	SF	GGBS	C	SF	GGBS		*x*	*y*	*z*
0.20	1.73	1.91	2.18	10.3	9.24	8.06	0.49	0.39	0.31	0.14	0.34	0.36	54.2	5.91	5.41	4.86
0.25	1.64	1.94	2.17	9.97	8.67	7.95	0.43	0.40	0.33	0.31	0.29	0.27	46.2	5.62	5.81	5.45
0.30	1.62	1.79	2.08	9.27	8.85	7.88	0.42	0.36	0.30	0.34	0.37	0.36	38.6	8.68	4.55	5.20
0.35	1.30	1.63	1.68	9.57	9.02	6.88	0.31	0.26	0.22	0.22	0.28	0.30	16.7	7.42	7.55	6.46
0.40	0.88	0.95	1.33	10.2	8.70	6.33	0.21	0.15	0.18	0.17	0.07	0.16	15.9	8.96	7.18	7.11
0.45	0.17	0.21	0.40	11.7	9.19	7.05	0.10	0.04	0.08	0.11	0.15	0.16	3.33	13.3	11.9	13.3
0.30*	0.30	0.21	0.33	112	73.0	106	0.17	0.07	0.12	0.15	0.18	0.08	-	-	-	-

***** Containing SRA

Table 7 Effect of maximum aggregate size (MSA: 5, 10, 20 mm) and binder type on the characteristics of autogenous shrinkage induced microcracks in 0.30 w/b concretes.

MSA	Vol. fraction (%)			Spec. surface (mm^{-1})			Average width (µm)			Average length (µm)			Density (mm/mm^2)			Anisotropy (-)		
	C	SF	GGBS	C	SF	GGBS	C	SF	GGBS	C	SF	GGBS	C	SF	GGBS	C	SF	GGBS
5	0.39	0.55	0.62	12.8	12.1	11.1	14.7	23.3	32.4	95	103	113	0.27	0.24	0.19	0.27	0.23	0.27
10	1.62	1.79	2.08	9.27	8.85	7.88	38.2	50.3	69.6	161	194	174	0.42	0.36	0.30	0.34	0.37	0.36
20	2.34	2.87	3.63	7.04	6.28	5.57	45.5	71.8	102.3	239	214	250	0.52	0.40	0.36	0.26	0.25	0.49

Fig. 1 Particle size distribution of coarse and fine aggregates.

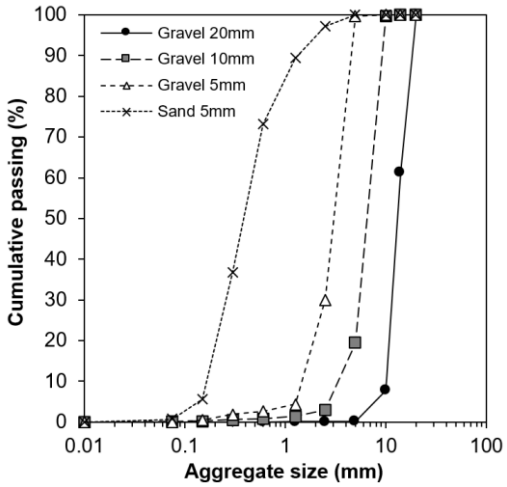

Fig. 2 Autogenous shrinkage (linear deformation) of concretes with different w/b ratios and binder types (a-c), and maximum size of aggregates (MSA, d).

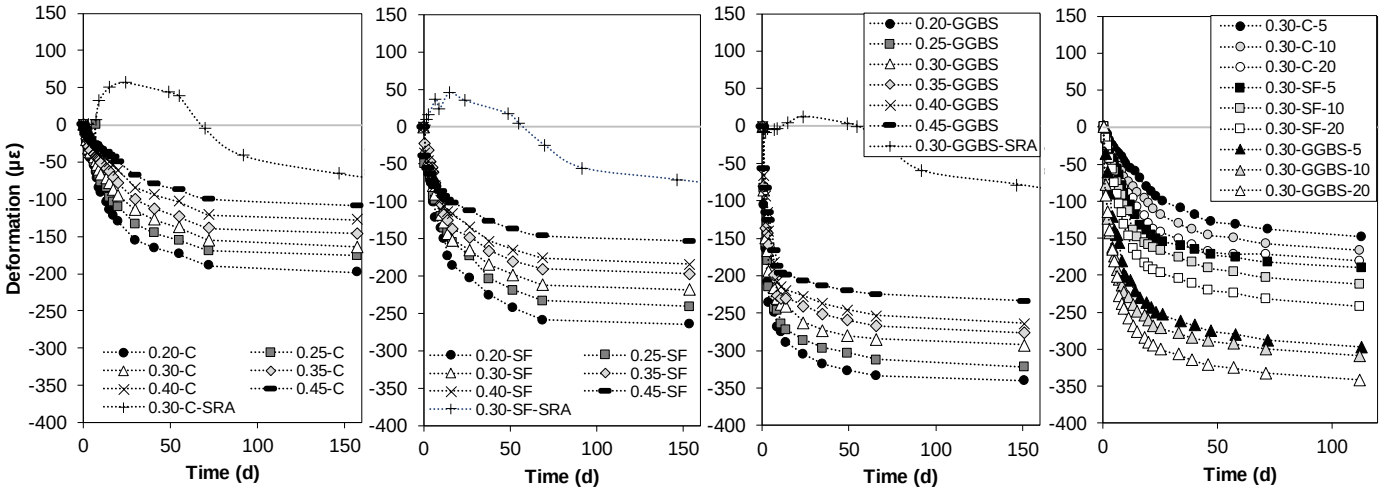

(a) CEM I (b) CEM I + 9%SF (c) CEM III (70% GGBS) (d) MSA

Fig. 3 Correlations between mass transport properties and autogenous shrinkage for concretes with different binder types and w/b ratio after 3.6 years sealed curing. Mixes containing shrinkage reducing admixture (SRA) are circled. Error bars represent ± one standard error.

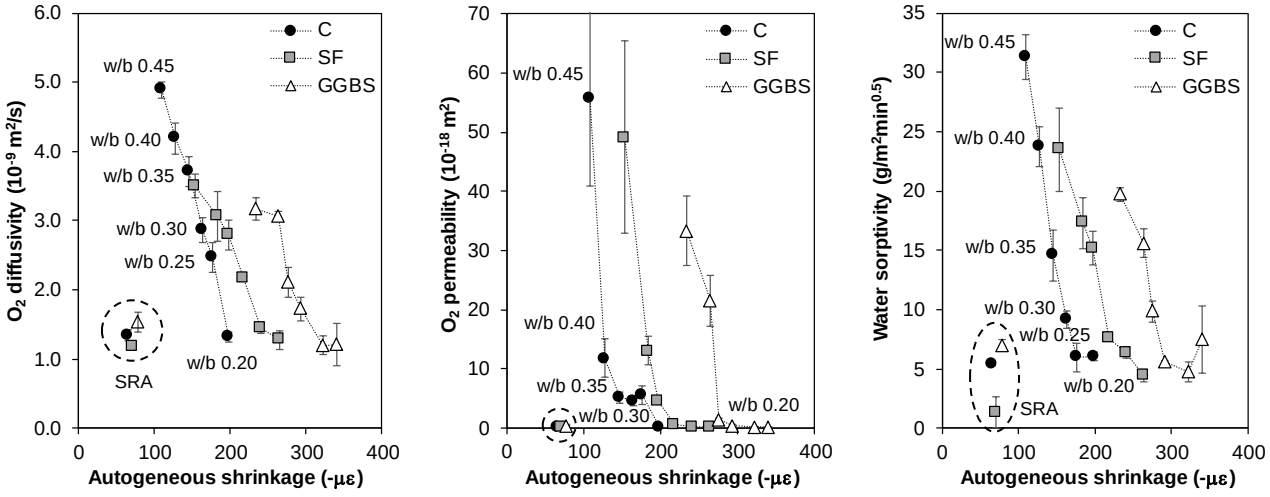

(a) Diffusivity (b) Permeability (c) Sorptivity

Fig. 4 Correlations between transport properties and accessible porosity for all samples after 3.6 years sealed curing. Error bars represent ± one standard error.

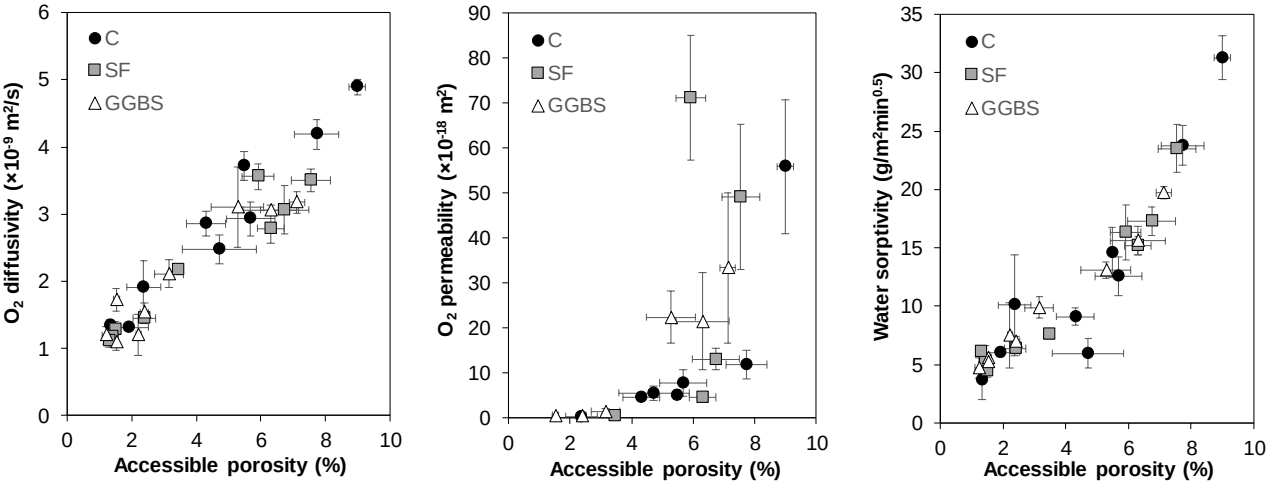

(a) Diffusivity (b) Permeability (c) Sorptivity

Fig. 5 Example LSCM images of SF-blended concretes. Mixes at lower w/b ratios showed less capillary porosity, but higher amounts of microcracking (arrowed).

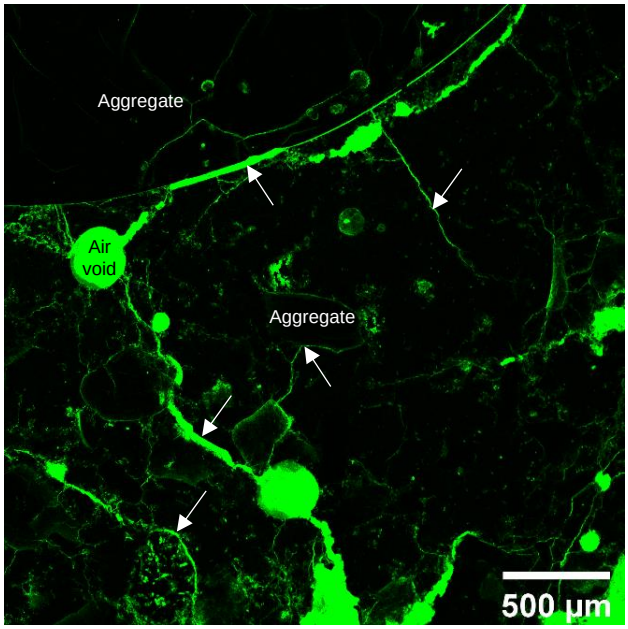

(a) 0.20-SF

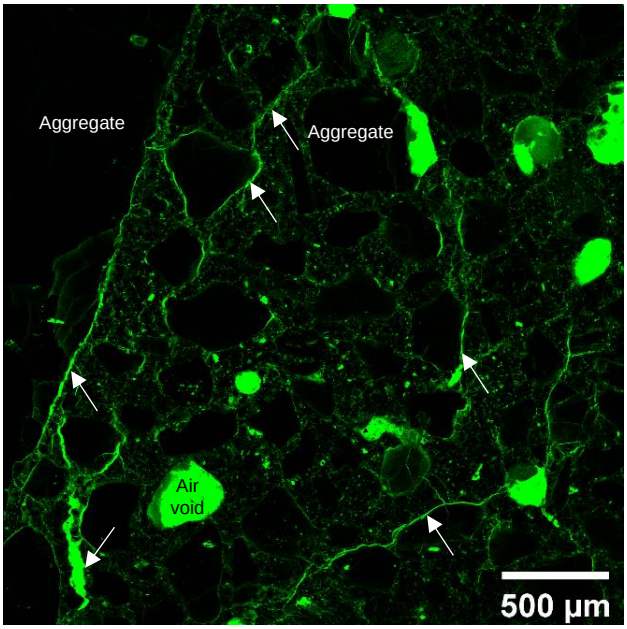

(b) 0.25-SF

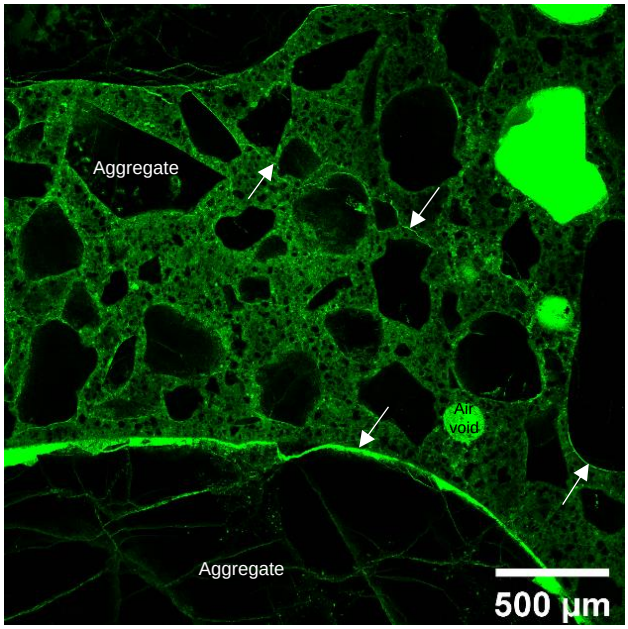

(c) 0.30-SF

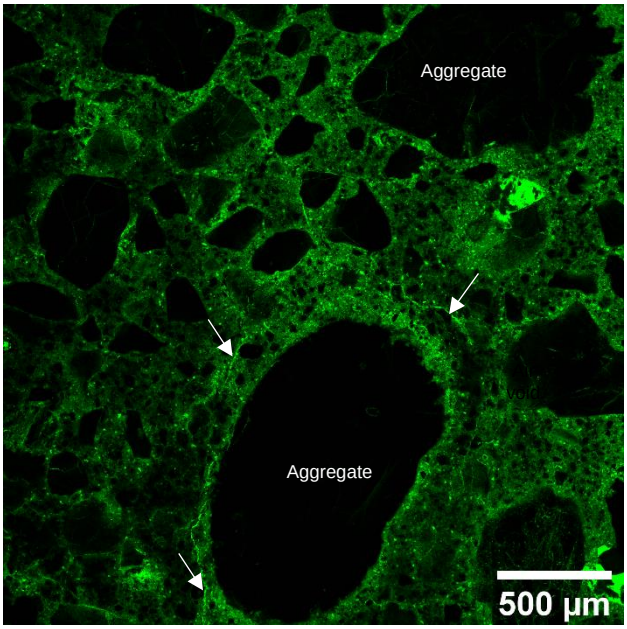

(d) 0.35-SF

Fig. 6 3D views of microcracks extracted from X-ray µCT images of silica fume-blended systems. Colour bars represent local thickness (microcrack width).

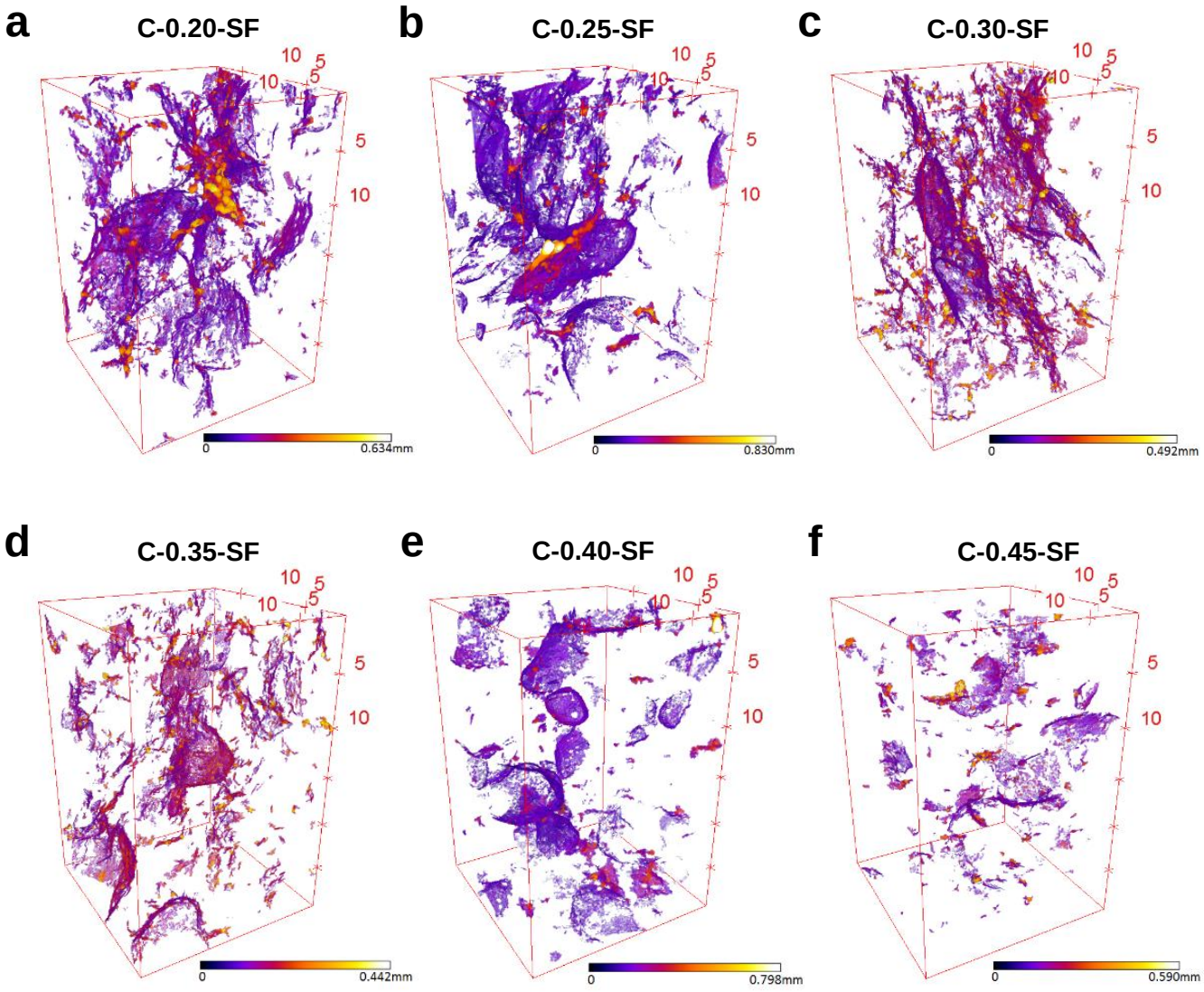

Fig. 7 Cumulative distribution of microcrack width (a) and length (b) measured on cross-section (65 × 95 mm) of concretes with different binder types and w/b ratios. Average values are indicated by markers.

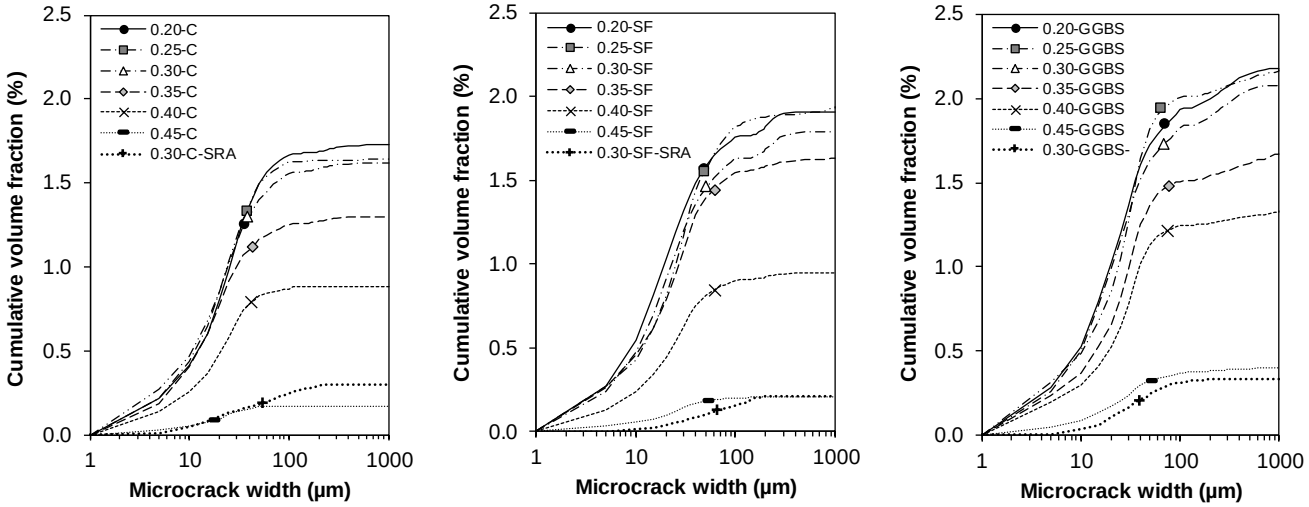

(a) Width distribution

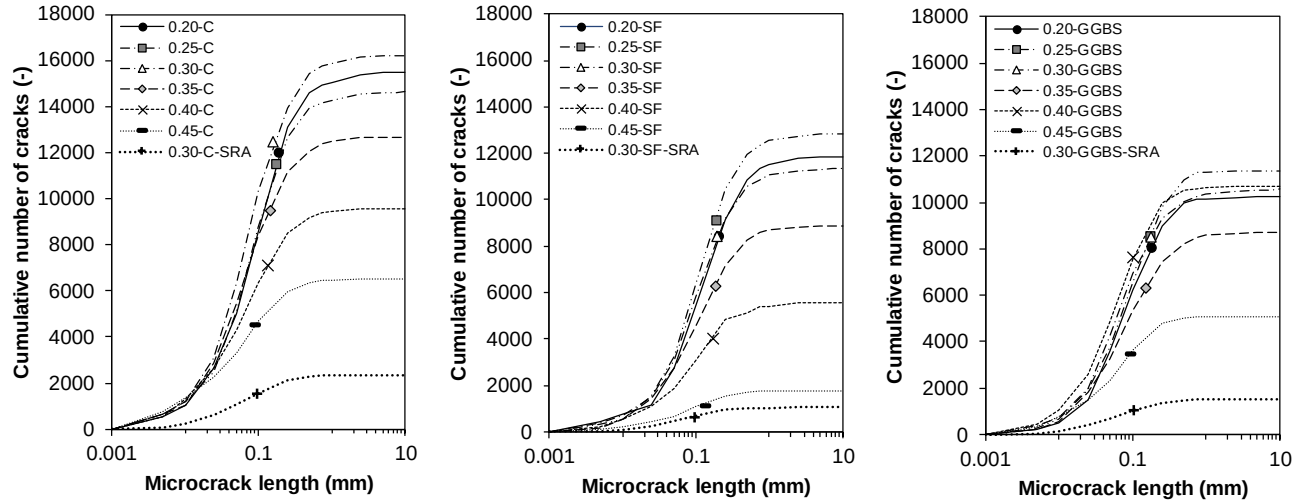

(b) Length distribution

Fig. 8 Relationships between microcrack volume fraction, autogenous shrinkage and accessible porosity for different binder types, w/b ratios (a, b) and maximum aggregate size MSA (c).

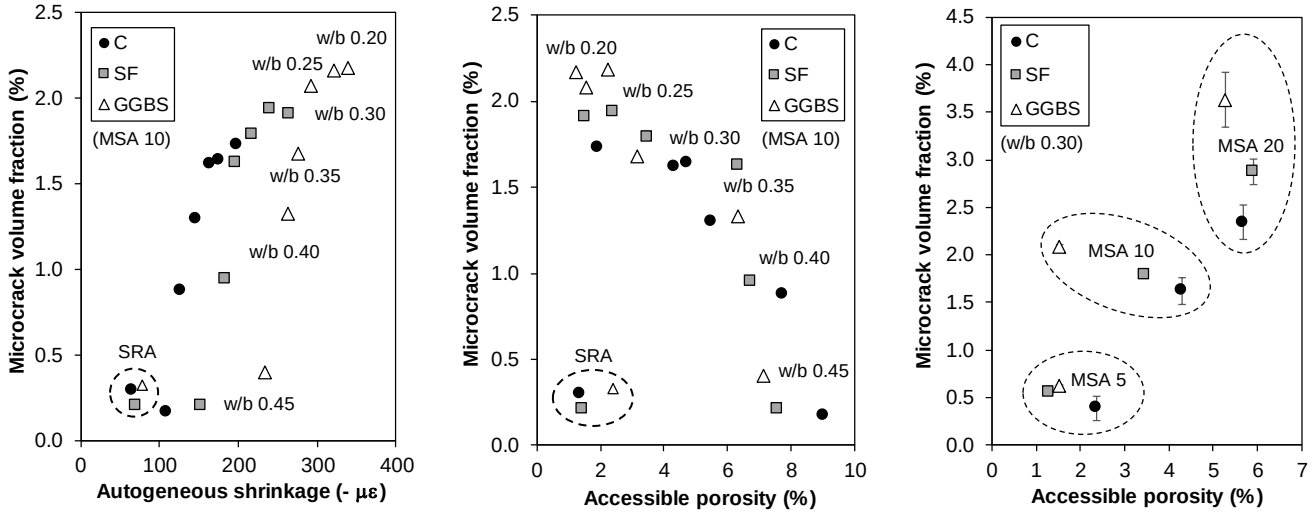

(a) (b) (c)